Multi-component lattice Boltzmann equation for mesoscale blood flow

2003 J. Phys. A: Math. Gen. 36 8517

(http://iopscience.iop.org/0305-4470/36/31/313)

INSTITUTE OF PHYSICS PUBLISHING JOURNAL OF PHYSICS A: MATHEMATICAL AND GENERAL

J. Phys. A: Math. Gen. **36** (2003) 8517–8534 PII: S0305-4470(03)58720-0

Multi-component lattice Boltzmann equation for mesoscale blood flow

M M Dupin, I Halliday and C M Care

Materials Research Institute, Sheffield Hallam University, Howard Street, S1 1WB, UK

Received 20 January 2003, in final form 3 June 2003
Published 23 July 2003
Online at stacks.iop.org/JPhysA/36/8517

Abstract

We present an improved lattice Boltzmann model of multi-component flow which permits practical, hydrodynamic modelling of multiple immiscible fluids. The model is robust and significantly reduces the interface anisotropy and micro-currents, which are artefacts observed in many schemes. Our new scheme is used on a particular regime of blood flow: that of the veinule mesoscale, where it is necessary to resolve significant numbers of deformable, interacting cells, which we model as incompressible liquid drops. We demonstrate the model's ability to recover the complex flow phenomena typical of the veinule scale.

PACS numbers: 02.70.−c, 47.11.+j

1. Introduction

Over the last decade, a range of lattice Boltzmann (lB) methods have been developed as mesoscopic models of isotropic [1] and anisotropic [2] fluids. The lB method shows particular promise when applied to complex flow at low Reynolds number [3] and especially to multi-fluid systems. A range of techniques have been developed to model fluid interfaces (e.g., [4–6]), with perhaps the Shan–Chen approach [7] being the most popular. More details can be found in reviews by Benzi *et al* [8] and Chen *et al* [9]. It is our objective here to demonstrate that a multi-component lB provides a basis for one particular model of veinule-scale flows. In section 2 we outline this 'explicit' model of mesoscale blood flow, in which we resolve deformable, advected blood cells as incompressible drops of many immiscible liquids.

It should be noted that even in mesoscale hydrodynamics the boundary between two immiscible fluids should have no structure or thickness. Surface tension is activated in lB by a number of methods which are *microscopically* physical. As a result, the emergent *continuum* interface suffers from unwanted artefacts: (i) small but spurious velocities, or *micro-currents*, and (ii) a finite thickness.

Key lB interface models are able to capture the kinematics of phase separation [5]. However, where hydrodynamics *alone* defines the problem narrow interfaces are desirable,

simply from the point of view of computational resources. This is especially true when the interfaces are intimate and the geometry is complex. Here we wish to simulate many immiscible, interacting drops. Computational considerations restrict the size of each. For hydrodynamic behaviour, graded interfaces of (say) width 6 lattice units on drops practically restricted to radius 20 lattice units are unphysical. Fortunately, in the hydrodynamic regime, simpler lB interface models [4] which produce a sharp interface (typically 2–3 lattice units) are as valid as any other lB method [10]. The basic technique of Gunstensen and Rothmann [4] is, moreover, the method most readily amenable to the algorithmic developments designed to accommodate mutually immiscible species (section 3.3).

To be precise, we base the work reported here on a version [6] of the interfacial model due originally to Gunstensen and Rothmann [4]. The use of a Gunstensen/Rothmann-type lB model is further justified by its ability to sustain a significant difference in kinematic viscosity between the separated liquids at low Re. The basic method is described in section 3.1 and refined in section 3.2, reducing both the anisotropy of the interface and the intensity of the micro-currents. The generalization of this model to any number of mutually immiscible species is then presented in section 3.3.

In section 4 we present quantitative results which demonstrate the improvements in the surface tension algorithm and results which demonstrate its ability to realize veinule-scale blood flow.

We present our conclusions in section 5.

2. Model for mesoscale blood flow

Blood flow has been studied for many years. The majority of studies deal with visco-elastic flow in vessels with a diameter more than two orders of magnitude greater than that of a red blood cell (RBC). Here blood is considered to be a homogeneous, non-Newtonian liquid (see Quarteroni [12]). There is also work on microscopic flows, where single cells are modelled explicitly (see below). In this case, the flow is recovered from low Re multi-component hydrodynamics in which the interface-mediated physics is of primary importance. Certain mesoscale calculations have 'resolved' cells by assuming that blood components advect along the streamlines of the corresponding undisturbed flow. Whilst limiting, this assumption is probably reasonable for small, rigid cells. However, when cells are of a size comparable with the vessel, explicit deformations and interactions cannot be neglected. A full understanding of such processes requires explicit modelling of a high volume fraction of deformable, and interacting, particles [11].

Microcirculation flows, in small veins or veinules, are characterized by significant numbers of strongly interacting cells, which require explicit resolution. Capillary length scales have flow dominated by plasma-advected RBCs and the crucial properties of constant RBC surface area and preferred membrane curvature are undoubtedly of central importance. But at the veinule scale there are a range of important phenomena, in which explicit models of deformable cells should be used, and where one expects membrane curvature to be less important than the volume exclusion effects associated with high cell numbers. We briefly discuss some examples of such situations:

(1) In veinules, white blood cells (WBCs) can concentrate near the walls. *Margination* can promote WBC function. Margination is affected by flow rate, WBC to RBC ratio and *haematocrit*, the latter being the percentage volume of solids in plasma, typically 37%. The mechanism which drives the RBC to migrate towards the centre of the vessel may be RBC aggregation, and associated volume exclusion effects, or it may also be their greater

deformability. Calculations have considered single solid cells but there are no results in the interface-dominated regime treating significant numbers of deformable particles.

(2) Empirically, haematocrit is found to be the principal determinant of blood viscosity. The investigation of haematocrit dependence of viscosity becomes possible only with an explicit model.

(3) Margination near a microcirculation junction causes plasma-rich blood in any side vessel [13]. This effect, known as plasma skimming, clearly requires explicit resolution of blood components and flow geometry.

Clearly, it would be valuable to have a model capable of resolving flow constitution, geometry, differential deformability (RBC versus WBC) and particle size distributions. So, for the type of applications outlined above, we propose an incompressible liquid drop model. Such a model must automatically capture the constraint of constant cell volume and allow for differential deformability. The constraint of constant cell surface area is assumed to be less important. In summary, we represent veinule-scale blood as a heterogeneous *liquid* consisting of a wetting, ambient plasma component and a number of intimate, approximately solid and mutually immiscible drops. The drops may have different sizes, viscosities and surface tensions for different applications.

Despite success over a range of applications, conventional computational fluid dynamics (CFD) is unsuited to model such flows as we propose here. However, lB offers a practical vehicle for our drop model of the veinule microcirculation. The multi-component lattice Boltzmann (lB) method has been used for flows containing separated liquids. However, to simulate the situations outlined in (1)–(3) above, one must have a means of interrupting coalescence/evaporation between drops. For, note, RBCs accrete at low shear into 'rouleaux' but certainly do not amalgamate like drops of oil in water. Therefore, to adapt lB for the veinule microcirculation it is necessary to devise a practical algorithm with controlled liquid drop coalescence. This is discussed in section 3.

To demonstrate its worth in situations such as (1)–(3), our model must work sensibly with many suspended drops, all of a size comparable to that of the veinule, all showing deformation. Using the N-phase lB (section 3), we simulate, in section 4, a dense suspension of relatively viscous, neutrally buoyant deformable cells. The cells are assumed to be advecting through an asymmetrically expanding duct at a Reynolds number—a situation representative of physiological flows. Crucially, the balance between inertial and surface tension forces (capillarity or Taylor number) is controlled so as to allow clear deformation in all parts of the flow.

3. Development of the lB model

We outline an lB model of multi-component flow for $\gg 2$ mutually immiscible species, designed to provide a vehicle for the modelling requirements outlined in section 2. For the reasons discussed in section 1, our liquid–liquid interface is generated by a version of the Gunstensen and Rothmann lB algorithm [4]. We further demonstrate that this interface has, for hydrodynamic applications, properties matching those of more popular lB interfaces [7].

As a basis we adopt the two-dimensional, 9-velocity LBGK model (denoted by $D2Q9$, with the $Q = 9$ velocities depicted in figure 1), which has a single scalar collision parameter. This was pioneered by Qian and d'Humières [18] and analysed in detail by Hou *et al* [15]. The lB model fluid is weakly compressible but for the envisaged range of Re, compressibility errors should be very small.

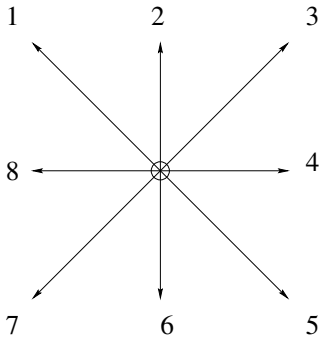

Figure 1. The D2Q9 lattice basis or velocity set used for our basic single relaxation time LBGK model.

3.1. An lB interface

We first consider two immiscible liquids. Our model currently applies to fluids with the same physical density. For small Re, the effect of gravity on differential drop buoyancy may be approximated through a body force, an approach which is exact only at $Re = 0$. However, buoyancy effects will not be of primary importance in the target blood flow application though they may be significant in other adaptations of our model. Hence we consider body forces in this subsection.

Vectors of the lattice basis are denoted as $\mathbf{c}_i$ with indexing given in figure 1. The collision, propagation and forcing of a D2Q9 LBGK algorithm is written as

$$f_i(\mathbf{r} + \mathbf{c}_i\delta_t, t + \delta_t) = f_i(\mathbf{r}, t) + \frac{1}{\tau}\left(f_i^{(0)}(\rho, \rho\mathbf{v}, t) - f_i(\mathbf{r}, t)\right) + F_i \tag{1}$$

where δ_t represents the time step, τ controls the molecular viscosity of the lattice fluid through

$$\nu = \left(\frac{2\tau - 1}{6}\right) \tag{2}$$

(units of the time step, δ_t) and the constant, F_i, represents a spatially *uniform* body force density which includes (i) parameter g, which differs for the two fluids and approximates the effects of buoyancy [17], and (ii) a term which represents an applied constant pressure gradient, G. The overall forcing, F_i, is thus

$$F_i = 3Gt_p\rho c_{ix} + 3gt_p\rho c_{iy} \tag{3}$$

where the weights, t_p, are defined below.

The macroscopic density and momenta of the two fluids are obtained from the moments

$$\rho = \sum_i f_i \qquad \rho\mathbf{v} = \sum_i f_i\mathbf{c}_i \tag{4}$$

and the equilibrium distribution function, $f_i^{(0)}$, is

$$f_i^{(0)}(\rho, \mathbf{v}) = t_p\rho\left[1 + \frac{\mathbf{v}\cdot\mathbf{c}_i}{c_s^2} - \frac{|\mathbf{v}|^2}{2c_s^2} + \frac{(\mathbf{v}\cdot\mathbf{c}_i)^2}{2c_s^4}\right] \tag{5}$$

with weights $t_p = 4/9, 1/9, 1/36$ for link index $i = 0$, i even, i odd, respectively (labelling of figure 1). $c_s = 1/\sqrt{3}$ is the velocity of sound for the D2Q9 model. The form of the equilibrium distribution function, (5), ensures that

$$\rho = \sum_i f_i^{(0)} \qquad \rho\mathbf{v} = \sum_i f_i^{(0)}\mathbf{c}_i \tag{6}$$

and also recovers the non-viscous components of the momentum–flux tensor through

$$\Pi^{(0)}_{\alpha\beta} = \sum_i f_i^{(0)} c_{i\alpha} c_{i\beta} = \frac{1}{3}\rho\delta_{\alpha\beta} + \rho v_\alpha v_\beta. \tag{7}$$

For a more detailed derivation of this basic algorithm see Zou *et al* [15].

Gunstensen and Rothmann [4] were the first to introduce multi-component behaviour into lB through the action of new rules added to a model similar to that outlined above. These new rules give a spontaneous interface between immiscible, *colour*-differentiated fluids, represented by momentum densities $R_i(\mathbf{r}, t)$ and $B_i(\mathbf{r}, t)$, as outlined in the next few paragraphs.

$R_i(\mathbf{r}, t)$ and $B_i(\mathbf{r}, t)$ are summed at each lattice node to define a conserved red density $\rho_R(\mathbf{r}, t)$ and a conserved blue density $\rho_B(\mathbf{r}, t)$, with $\rho(\mathbf{r}, t) = \rho_B(\mathbf{r}, t) + \rho_B(\mathbf{r}, t)$. $R_i(\mathbf{r}, t)$ and $B_i(\mathbf{r}, t)$ evolve as follows.

The overall, *colour-blind*, momentum density,

$$f_i(\mathbf{r}, t) = R_i(\mathbf{r}, t) + B_i(\mathbf{r}, t) \tag{8}$$

is used to calculate an overall density and velocity. These quantities are interpreted as the total density and velocity of the red and blue fluids at position $\mathbf{r}$, time t. A colour-blind equilibrium $f_i^{(0)}$ is then defined using equation (5). Collision of the multi-component fluid is performed in three steps: (i) a colour-blind collision using equations (5) and (1), (ii) a perturbation which introduces interfacial tension and (iii) a re-allocation of colour (*re-colouring*) which introduces component segregation.

Surface tension is introduced by inserting a small (nominally $O\left(\delta_t^2\right)$ [6]) mass and momentum conserving perturbation, Δf_i, to the post-collision $f_i(\mathbf{r}, t)$ prior to re-colouring:

$$\Delta f_i(\mathbf{r}, t) = \sigma C(\mathbf{r}, t) \cos(2(\theta_f(\mathbf{r}) - \theta_i)). \tag{9}$$

Here, the parameter σ controls the strength of the effective surface tension, angle θ_i is the angular orientation of lattice link i (figure 1) and $\theta_f(\mathbf{r}, t)$ is the direction of the colour gradient:

$$\mathbf{f}(\mathbf{r}, t) = \sum_{ij} (R_j(\mathbf{r} + \mathbf{c}_i, t) - B_j(\mathbf{r} + \mathbf{c}_i, t))\mathbf{c}_i \tag{10}$$

which is taken as an approximation to an interface normal at the boundaries between the two fluids. $C(\mathbf{r}, t)$ is a *concentration factor*:

$$C(\mathbf{r}, t) = 1 - \left| \frac{\rho_R(\mathbf{r}, t) - \rho_B(\mathbf{r}, t)}{\rho_R(\mathbf{r}, t) + \rho_B(\mathbf{r}, t)} \right| \tag{11}$$

which limits activation of surface tension to multi-coloured nodes [6].

Colour is de-mixed by re-allocating colour densities $\rho_R(\mathbf{r}, t)$ and $\rho_B(\mathbf{r}, t)$ over the post-collision 'receptacle' $f_i(\mathbf{r}, t)$ so as to maximize the work done by colour flux:

$$\mathbf{q}(\mathbf{r}, t) = \sum_i (R_i(\mathbf{r}, t) - B_i(\mathbf{r}, t))\mathbf{c}_i \tag{12}$$

against the colour gradient (10).

Different relaxation parameters τ can be applied to the separated liquids, to give them different kinematic viscosities. In the mixing/segregating region an effective relaxation parameter τ_{eff} is used, which, through identity (2), gives the appropriate mean viscosity for the fluids mixing at the interface:

$$\nu_{\text{eff}} = \frac{1}{6}(2\tau_{\text{eff}} - 1) = \left(\frac{\rho_R}{\rho_R + \rho_B}\right)\nu_R + \left(\frac{\rho_B}{\rho_R + \rho_B}\right)\nu_B. \tag{13}$$

Segregation and surface tension is thus produced in any region of the lattice where colours mix. Such a region corresponds to a fluid–fluid interface, with essentially correct continuum length scale properties [6]. Finally, it is important, for present applications, to note that the interfacial region is relatively narrow.

3.2. An lB interface with reduced micro-currents

It is possible to improve the properties of the emergent interface described in section 3.1. For given values of σ and τ, macroscopic interfacial tension in the 'diphasic' model (section 3.1) can be calculated for two interface orientations [16]. Surface tension for an lB interface parallel to the short link direction (even i, figure 1) is, to first order in product $\sigma\tau$ [16],

$$\Sigma_s = \frac{4\sigma\tau}{3}. \tag{14}$$

For an interface parallel to a long link direction (odd i, figure 1), we have a surface tension

$$\Sigma_l = \frac{4\sigma\tau}{\sqrt{2}}. \tag{15}$$

This difference holds a clue to the minimization of the micro-current.

The form of the perturbation we choose in equation (9) allows one to set surface tensions Σ_s and Σ_l independently. That is, perturbations applied to the odd i and even i $f_i(\mathbf{r}, t)$, will separately control Σ_l and Σ_s. This may be seen, for example, by considering an interface oriented parallel to the long links (odd i, figure 1). The value of perturbation (9), for all even i value $f_i(\mathbf{r}, t)$, is zero. Hence, all even i value $f_i(\mathbf{r}, t)$ are ignorable when considering Σ_l. An equivalent argument follows for Σ_s. Accordingly, we set Σ_s and Σ_l independently, using different perturbation parameters, σ and $\lambda\sigma$, to perturb even i and odd i value $f_i(\mathbf{r}, t)$. By adjusting λ, the closed interface bounding a red drop can be characterized by a single, uniform macroscopic surface tension. Dividing equations (14) and (15), we can estimate a value of λ to first order in the product $\sigma\tau$ [16]:

$$\lambda = \frac{3}{\sqrt{2}} \approx 2.15. \tag{16}$$

Ensuring that interfacial tension is uniform has other beneficial effects besides making a static drop more isotropic (circular). The interfacial micro-current field associated with a drop placed centrally on a lattice, bounded with no-slip walls, represents a solution of the Navier–Stokes equations with boundary conditions determined by the walls and by the velocities induced near to the interface by the segregating flux of the interfacial perturbation. The qualitative features of the micro-current flow field may be predicted by considering the directions in which the segregating flux has its maxima and minima. Hence, by smoothing the variation of this quantity with angular position, we also smooth the imbalance responsible for driving a micro-current. Accordingly, adjusting the ratio 16 should improve drop isotropy and minimize the micro-current activity, as measured by the velocity residual:

$$m = \sum_{\mathbf{r}} v(\mathbf{r}, t). \tag{17}$$

3.3. N immiscible fluids in lB: coalescence and wetting

Sections 3.1 and 3.2 introduce our lB model of a binary liquid. Here we generalize that model to a mixture of N immiscible liquids which must not coalesce or evaporate and which must have controlled wetting properties.

Hence, there are certain essential requirements in the N-colour extension. To regulate evaporation masses of individual drops each need to be conserved. Over 10^6 lattice updates, our interface algorithm in section 3.2 conserved the mass of a drop to better than $2.0 \times 10^{-3}\%$. Interruption of coalescence is just as crucial to model blood cells. The latter is quantified, for this algorithm, below. To avoid the need to consider cells' interaction with the veinule wall, we choose to prevent all drops from wetting the solid boundaries.

Our generalization to N immiscible components assigns each fluid a 'colour' superscript, $\alpha = 0, 1, 2, 3, \ldots, (N-1)$. Fluids with different values of α can have different properties, e.g., collision parameters, τ_α. Now, for N different species, multi-component lB quickly demands unviable amounts of computer storage, as N increases. But for relatively small, non-evaporating, 'sharp', drops, these arrays for N primary quantities $f_i^\alpha(\mathbf{r}, t)$ will be very sparse. Moreover, a natural question arises around the validity of attempting to represent, on lattice nodes with Q links or velocities (see figure 1), more than Q different colours or species.

To address storage, we track only N_Q ($< Q \ll N$) dominant species at any node. Note also that the particular N_Q colours, or immiscible components, vary between nodes. We are thus considering colour *difference*, as opposed to absolute colour, which is the source of the principal reduction in the requisite storage. The sharp interfaces from our Gunstensen-type interface method mean minimal mixing and a reduction in the number of different colours found on a node. In practice we take $N_Q = 5$. This value is found to be adequate for even the most intimate mono-disperse multi-component flows. But, note, this choice reflects the geometry and number of components (colours/drops) in our particular application.

Before further detailing our method, we acknowledge that, to guide species segregation, a lattice map of absolute colour is needed. However, for such a map, sufficient information can be stored in a four-dimensional array of integer type, with a subscript set $\{x, y, i, N_Q\}$ to identify, for lattice position $\{x, y\}$, direction i, the colours ($\leqslant N_Q$ in number) present their integer superscript, α. By recording N_Q species at each node, the dominant-type real storage requirements, on the primary quantity $f_i^\alpha(\mathbf{r}, t)$, for a total of N_0 drops (or immiscible components), is reduced by a factor N_Q/N_0, in fact to levels comparable with the diphasic model (below).

Controlling coalescence amounts to dealing consistently with all possible mixed node states, with a generalized perturbing and re-colouring processes, designed to eliminate mixing between all species. This requirement may still be stated as a need to maximize the work done by a generalized colour flux against a generalized colour gradient.

The diphasic colour gradient (section 3.1) must be generalized. We continue to assume that colour gradient defines an interface normal [20], and generalize it, based upon section 3.1. We define an interfacial colour gradient between any pair of de-mixing immiscible components, denoted by α and β, relative to the vector

$$\mathbf{I}_{\alpha\beta}(\mathbf{r}) = \sum_i \sum_j \left(f_j^\alpha(\mathbf{r} + \mathbf{c}_i) - f_j^\beta(\mathbf{r} + \mathbf{c}_i) \right) \mathbf{c}_i \tag{18}$$

which, we emphasize again, is assumed to be normal to the local (α, β) interface. This colour gradient is used to perturb the 'colour-blind', total:

$$f_i(\mathbf{r}, t) = \sum_{\alpha=0}^{N_Q - 1} f_i^\alpha(\mathbf{r}, t)$$

with a surface tension inducing perturbation. Note that this summation is on α: the corresponding summation of i gives the total density of fluid α on the node:

$$\rho_\alpha(\mathbf{r}, t) = \sum_{i=0}^{Q} f_i^\alpha(\mathbf{r}, t).$$

For the interface between components α and β we use a generalized perturbation after section 9:

$$\Delta f_i^{\alpha\beta}(\mathbf{r}, t) = \sigma_{\alpha\beta} C_{\alpha\beta}(\mathbf{r}, t) \cos(2(\theta_I(\mathbf{r}) - \theta_i)) \tag{19}$$

in which there is no summation on repeated subscripts, $\sigma_{\alpha\beta}$ is a surface tension parameter for the $\alpha\beta$ interface, θ_I is the polar angle of the field in equation (18) and

$$C_{\alpha\beta}(\mathbf{r}, t) = 1 - \left| \frac{\rho_\alpha(\mathbf{r}, t) - \rho_\beta(\mathbf{r}, t)}{\rho_\alpha(\mathbf{r}, t) + \rho_\beta(\mathbf{r}, t)} \right| \tag{20}$$

is the concentration factor for the (α, β) fluid pair, after equation (11). For a D2Q9 lattice, $\sigma_{\alpha\beta}$ is modulated by the factor λ (section 3.1), so that $\sigma_{\alpha\beta}$ becomes

$$\sigma_{\alpha\beta}^i = \begin{cases} \lambda\sigma_{\alpha\beta} & i \text{ even} \\ \sigma_{\alpha\beta} & i \text{ odd.} \end{cases}$$

The perturbations described in equation (19) are superposed for each of the $\leqslant {}_2P_Q$ fluid pairs (α, β) on a mixed node. This yields an effective perturbation to the colour-blind $f_i(\mathbf{r}, t)$:

$$\Delta f_i(\mathbf{r}, t) = \sum_{(\alpha\beta)} \Delta f_i^{\alpha\beta}(\mathbf{r}, t)$$

in which the summation is taken over all pairs (α, β) of fluids present (see below).

We now define an 'average' colour gradient which points towards component α and away from the total of all other components present at the node at $\mathbf{r}$:

$$\begin{aligned} \mathbf{f}^\alpha(\mathbf{r}) &= \sum_i \sum_j \left[f_j^\alpha(\mathbf{r} + \mathbf{c}_i) - \sum_{\beta \neq \alpha} f_j^\beta(\mathbf{r} + \mathbf{c}_i) \right] \mathbf{c}_i \\ &= \sum_i \sum_j \left[2 f_j^\alpha(\mathbf{r} + \mathbf{c}_i) - f_j(\mathbf{r} + \mathbf{c}_i) \right] \mathbf{c}_i . \end{aligned} \tag{21}$$

The same calculation is repeated for each fluid component present at the node, position $\mathbf{r}$. The appropriate colour gradient $\mathbf{f}^\alpha(\mathbf{r})$ (equation (21)) is used to re-colour for component α within each node in the same way as for a binary fluid.

The process defined above opposes the inter-diffusion of all different components. Note that to calculate the colour gradient (21) requires knowledge of the absolute colour, not just the relative amounts of the different colours present in a local environment. We also note that the sum on α of these individual fields is a measure of the local gradient in the total fluid density and is therefore zero only in a uniform fluid.

In order to achieve full colour separation, the order of the re-allocation of more than two colours to receptacle f_i is significant. Different ordering in the re-colouring process can clearly result in small differences in the post-collision post-segregated state. Careful observation shows that these differences are small but not without consequence. They are, for example, probably linked to the residual micro-current activity. In order to produce optimum segregation (sharp interface), the minority species at a node is given *priority* allocation to its favoured direction. Failure to adopt this scheme results in a relatively large loss of information about the location of minority species, resulting in increased drop evaporation.

Target flow applications are, by intention, heavily interface dominated. Recall, for our effectively mono-disperse systems here, a maximum of five drops in proximity were allowed (again, simple packing considerations mean this value will increase with increasing polydispersity). Five immiscible drops or de-mixing fluids lead to ${}_2P_5 = 10$ *possible* local interfaces. This factor 'amplifies' the computational overhead attending the increase in the total length of interface as N (drop number) increases, as assessed in table 1 (see below).

Table 1. The dependence of the memory of the algorithm and execution speed (times) upon N, number of immiscible drops (fluids), based upon a 100 lattice updates on a 200 × 200 square lattice. The drop size varies (decreases) as N increases.

N	2	10	100	1000
Time (min)	7	8	9	11
Memory (Mb)	64	64	64	64

Table 2. The dependence of the memory of the algorithm and execution speed (times) upon N, number of immiscible drops (fluids), based upon a 100 lattice updates on a 200 × 200 square lattice. The drop size remains fixed as N increases, hence the constrained range of parameter N.

$N = N_Q$	2	3	4	5	6	7	8	9
Time (min)	1.1	1.5	1.8	2.1	2.3	2.6	3.0	3.4
Memory (Mb)	10	12	14	16	18	20	22	25

We now proceed to consider the wetting properties of our algorithm. To bound a mixture of suspended drops in an internal flow we must consider the relative wetting properties of the liquids, and we now describe a means of controlling continuum-scale inter-component and wall-wetting properties.

Consider a mixture of fluids close to a boundary. Differential wetting is achieved using a perturbation process similar to that used for liquid–liquid wetting. Accordingly, the wall-wetting perturbation for a fluid α is taken to be

$$\Delta f_i^\alpha(\mathbf{r}, t) = \rho^\alpha(\mathbf{r}) \cos(2(\theta_w(\mathbf{r}) - \theta_i))\sigma_{\alpha|\text{wall}} \tag{22}$$

where $\rho^\alpha(\mathbf{r})$ is the wall-nodal density of the fluid α, $\theta_w(\mathbf{r})$ is the orientation of of the wall normal and $\sigma_{\alpha|\text{wall}}$ is a parameter controlling the 'wetting surface tension' of the fluid α. By setting different values of $\sigma_{\alpha|\text{wall}}$, the different components present at a boundary may each be differently inclined to wet. Different components therefore compete to wet the boundary, which is the essence of the underlying physical process. The perturbations described in equation (22) are repeated (superposed) for each fluid α on a mixed wall node.

Results of wall-wetting simulations are presented in section 4. These show the change in shape of a drop at a wall as a result of variation in the wetting parameter. The wall perturbation process is found correctly to control the wetting at the boundary, and this leads to a wide range of possible applications. For the present, we wish simply to ensure that the 'plasma' preferentially wets the boundary, thereby denying adhesion of the red blood cell drops and maintaining an explicitly resolved layer of plasma at the boundary. Thin films of incompressible liquid at low Re (the 'lubrication regime') can sustain large hydrostatic pressures. An explicitly resolved layer of plasma also avoids the need to postulate the sub-lattice 'lubrication force' associated with narrow contacts in the lubrication regime. We note that white-cell adhesion could also be easily incorporated using the methods just described.

Tables 1 and 2 summarize the performance of our algorithm executed on a Silicon Graphics Origin 300 500 MHz IP35 (CPU: MIPS R14000) workstation. Table 1 shows the dependence of the memory requirements of the algorithm and execution time upon N, number of immiscible drops (fluids), based upon a 100 lattice updates on a 200 × 200 lattice, with the drop size decreasing as N increases, note. The information in table 1, which assumes a maximum of five colours or immiscible components per node *for all values of* N, emphasizes that the total memory requirement is tied to the choice of N_Q (=5, recall), number of 'recognized components' and therefore it does not scale with N. The execution time increases in proportion to the total length of all interfaces, although this is not apparent in the data of table 1, because of the particular way that the drop size is reduced as N is increased, (to assist packing).

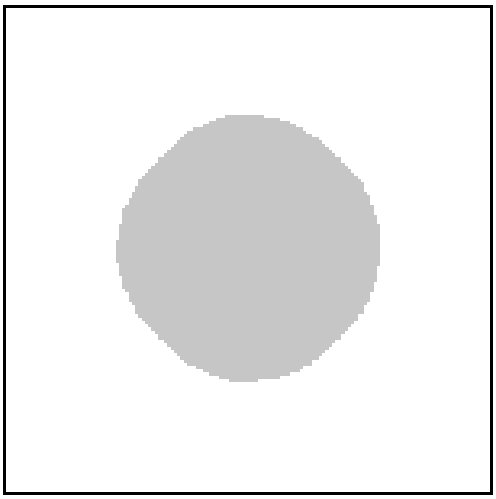

a(i)

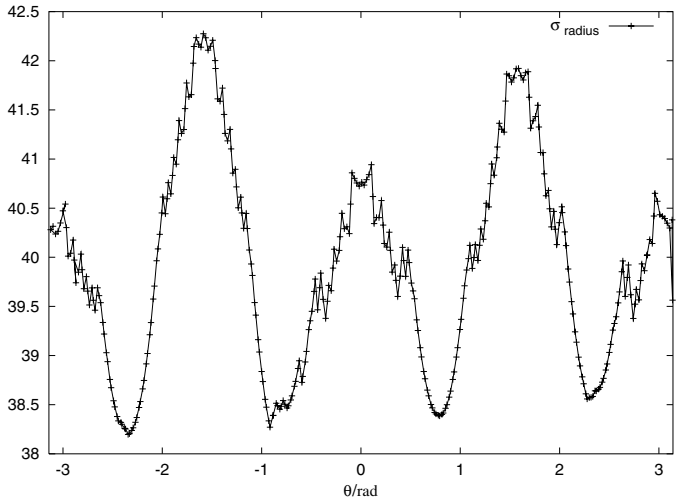

a(ii)

Figure 2. Results performed on a 150 × 150 lattice with drops initialized to radius 40 lattice units. The images *a*(i), *b*(i) and *c*(i) show the shape of the interface for the different values of λ: λ = 1.0 (too small), λ = 2.1 (close to optimum) and λ = 4.0 (too big). The corresponding plots *a*(ii), *b*(ii) and *c*(ii) show drop radius as a function of angular position in the interface. The optimum value of the parameter λ occurs close to the predicted value (2.15) obtained from equation (16).

Table 2 shows the dependence of the memory of the algorithm and execution time upon $N = N_Q$, based upon a 100 lattice updates on a smaller 100 × 100 lattice, now with the drop size fixed as N increases over a smaller range. Unsurprisingly, given these conditions, the execution times and memory requirements in table 2 both increase in proportion to $N = N_Q$.

4. Validation and application of the lB model

In this section we first describe the validation of the improved lB interface followed by simulation results typical of the veinule-scale microcirculation. In respect of the latter, we

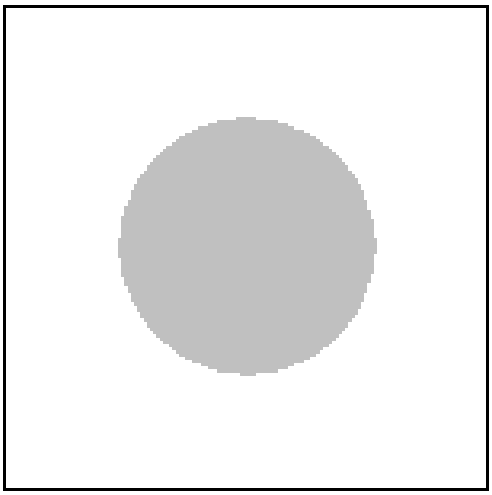

b(i)

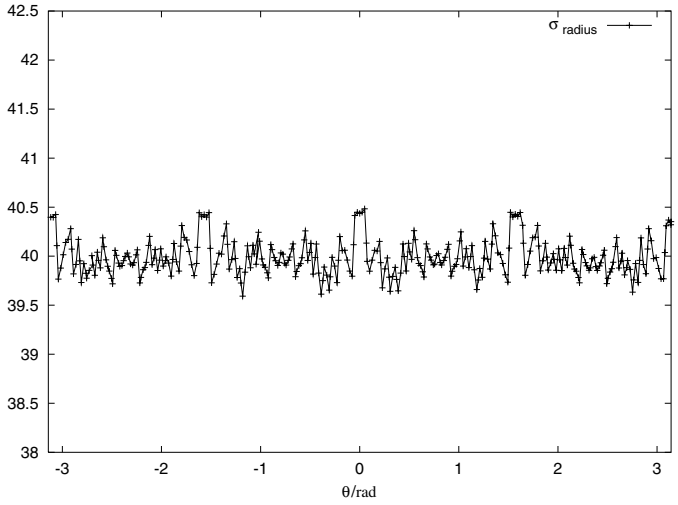

b(ii)

Figure 2. (Continued.)

consider (i) single advecting, deforming drops, (ii) control of coalescence and (iii) many immiscible, deformable drops.

Note that the contact angle for three components α, β and γ in contact may be compared with its value from Young's equation:

$$\cos(\theta_e) = \frac{\gamma_{\alpha\gamma}}{\gamma_{\alpha\beta} + \gamma_{\beta\gamma}} \tag{23}$$

in which $\gamma_{\alpha\beta}$ is the macroscopic $\alpha\beta$ surface tension, proportional to $\sigma_{\alpha\beta}$.

4.1. Drop interface

Simulations reported here refer to a lattice fluid nominally at rest, initialized to an equilibrium state of uniform density $\rho = 1.80$ on a 150×150 lattice with a drop of initial radius 40 lattice units. Evolution was performed to steady state. The interface and lattice collision parameters

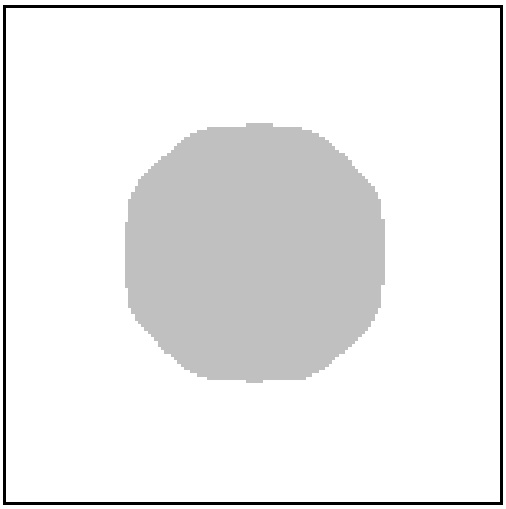

c(i)

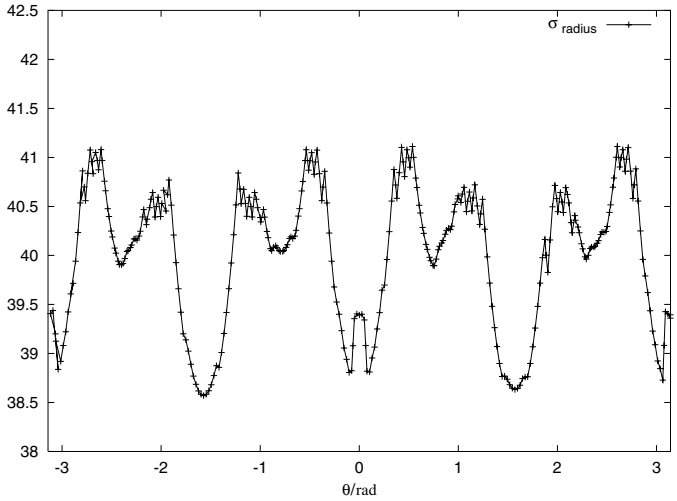

c(ii)

Figure 2. (Continued.)

were 0.0075 and 1.7, respectively. Micro-current activity and isotropy were assessed at each time step by the scalar lattice summation of the velocity residual (equation (17)). This quantity was used to identify the steady state and the results were obtained for a wide range of ratio parameter λ.

Drop isotropy is measured in graphs of the drop radius (distance from the centre of mass to multi-coloured sites in the interface) as a function of angular position. Figures 2*a*(i), *b*(i) and *c*(i) depict the position of the interface for $\lambda = 1.0$ (too small), $\lambda = 2.1$ (close to optimum) and $\lambda = 4.0$ (too big) and the corresponding plots *a*(ii), *b*(ii) and *c*(ii) represent drop radius with angular position. The increased range and resolution of λ shown in figure 3 confirms the trend. Figure 3 shows two sets of data, each normalized to its value at parameter $\lambda = 2.15$. The first set (circles) shows the standard deviation of the drop radius, the second (triangles) shows the micro-current activity measured by the parameter m (equation (17)). Both series

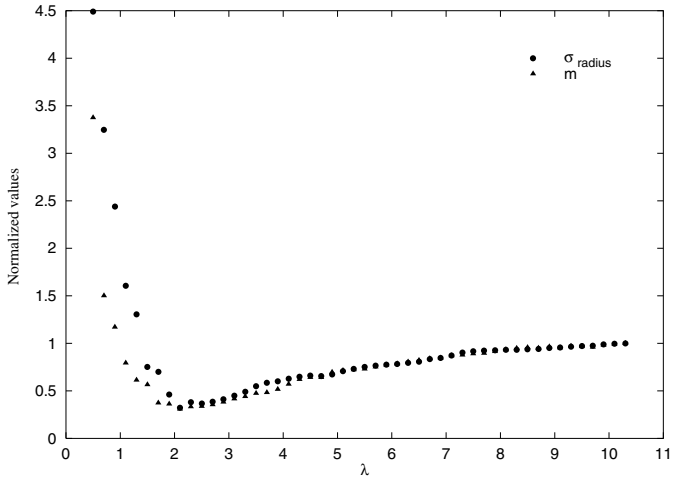

Figure 3. The standard deviation of a drop radius (circles) normalized to its value at parameter $\lambda = 2.15$ and the micro-current activity m (triangles) again normalized to their value at $\lambda = 2.15$. All data correspond to a value of $\sigma = 7.5 \times 10^{-3}$ and LBGK collision parameter $1/\tau = 1.7$. Note the coincident and pronounced minimum at the expected value, $\lambda \approx 2.15$, in both series of data.

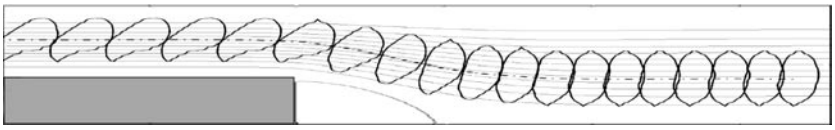

Figure 4. Instantaneous drop configurations for a drop entrained in flow past an asymmetric expansion, superimposed over shows streamlines from the corresponding undisrupted (single phase) flow. Note that the lowest resolved streamline in figure 3, immediately to the left of the step corresponds to a recirculation.

of data show a pronounced minimum at the expected value, $\lambda = 2.15$. The optimum circular shape occurs when parameter λ is close to the value predicted from equation (16) and in this case anisotropy in the radius cannot be resolved.

Careful measurements around $\lambda = 2.1$, based upon the standard deviation of the radius, reveal weak dependence of optimum λ upon the value of LBGK relaxation parameter τ. This is understandable, since the theory behind equation (16) is only first order in product $\tau\sigma$ [16].

4.2. Deforming, advecting drop

For definiteness, we take an asymmetrically expanding duct. A number of detailed, physiologically relevant questions arise around this geometry (figure 4), e.g., for given *Re*, what size of drop can become trapped in any feature corresponding to a primary vortex of the undisturbed flow? Our aim here is to demonstrate the potential of our lB simulation in such problems.

In the results presented here, the effects of gravity are ignored. Although the effects of gravity are not important in most mesoscale blood flow applications, it is still possible to approximate the influence of gravity by the use of different constants g in the evolution (equations (1) and (3)). Flow was forced by a constant body force, G (equation (3)), applied uniformly to both fluids. The step was simulated as adjacent front-facing and back-facing steps in a channel with periodic boundary conditions in the horizontal direction. Figure 4 shows

results only from the back-facing region, which might be taken to represent the occlusion of a vessel caused by the accumulation of plaques at its wall. Single drops were entrained by an effective pressure gradient. The expansion has a ratio of step height to upstream throat of $1/3$ and the narrow part of the channel was resolved to 40 lattice units (lu), which are defined to be the shortest inter-node distance. The Reynolds number for the corresponding undisturbed flow was set at a physiologically representative, $Re = 73$.

We now consider drop deformation in more detail. Red blood cells change shape in response to local flow conditions and, in turn, deformation affects the physiological function of the red cells. Moreover, at a concentration of 50% by volume, a suspension of solid spheres cannot flow, whereas blood is fluid even at 98% concentration by volume. Clearly it is essential to capture deformation. To assist, we appeal to a lattice capillarity or Taylor number:

$$Ca = \frac{\gamma \nu R \rho}{\Sigma} \tag{24}$$

where γ is the local shear rate, R is the undeformed drop radius and ν is the kinematic viscosity of the liquid of the drops. Figure 4 superimposes snapshots of a reasonably deformable drop over the streamlines of the corresponding undisturbed flow. The Taylor number was set at $Ca = 0.04$ and the initial radius 7 lu. This choice of Ca was made in order to produce a drop deformation similar to that photographed for a red blood cell deforming in a hydrodynamic focusing experiment [19].

By adjusting the collision parameter of the drop fluid in the range $0.4 < \tau < 1.99$, it is possible to obtain a drop/fluid viscosity ratio up to approximately 300. However, for all our results, this viscosity ratio is set to be 7, which is approximately the correct ratio for the viscosity of the internal fluid of red blood cells by comparison with the surrounding plasma. These arguments clearly ignore the effects of the elastic properties of the cell membrane which we have assumed to be less important in the class of flows we consider. Note also that the lowest value of resolved streamline in figure 4 is actually recirculating.

4.3. Many deforming, advecting drops: blood flow

In high volume fraction flows, drops can come close to the simulation boundary. To avoid the need to postulate sub-lattice lubrication forces, we always encourage an explicit layer of plasma fluid to remain between drops and the boundary. We need to ensure preferential wetting of the boundary by the plasma fluid and this requires control over contact angle. Before proceeding to consider applications and results for veinule-scale simulation, we must therefore verify the wetting behaviour of our lB algorithm.

To demonstrate our liquid–liquid wetting algorithm (section 3.3), figure 5 shows typical results obtained for three static, immiscible fluids on a lattice, dimension 150×50, reciprocal collision parameter $1/\tau = 1.7$. This data was obtained by assigning a range of different values to the respective surface tensions. A circular arc has been fitted through the set of mixed nodal densities to obtain the interface fit and hence θ_e. Each of the interfacial points in figure 5 lies $<$10th lu from the fitted circle. Results in figure 5 are in excellent agreement with the expected values; the difference between the measured and expected contact angles (equation (23)) evaluates to $<2\%$.

In respect of liquid-boundary wetting, simulation results achieve the similar degree of agreement. However, the shapes of the drops at a solid surface (figures 6) are not so circular; the fit shows an average of $\approx$0.5 lu between the fit and the interpolated interface. This discrepancy is due to the cumulative effect of the micro-current at the simulation walls, which drives very small circulations sufficient to disturb the drops in a rest simulation. However, these effects are small and normally overwhelmed by flow.

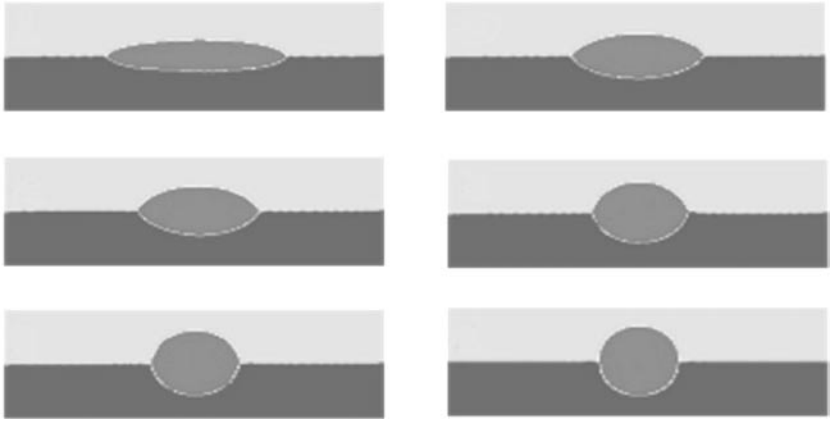

Figure 5. Results obtained for three immiscible fluids at three different relative surface tensions, chosen so as to vary the resulting contact angle. Data shown derive from a simulation of 10^5 time steps, on a lattice, dimension 150×50, again with collision parameter $1/\tau = 1.7$ (all fluids). Measured contact angle values may be compared with the theoretical values given by Young's equation.

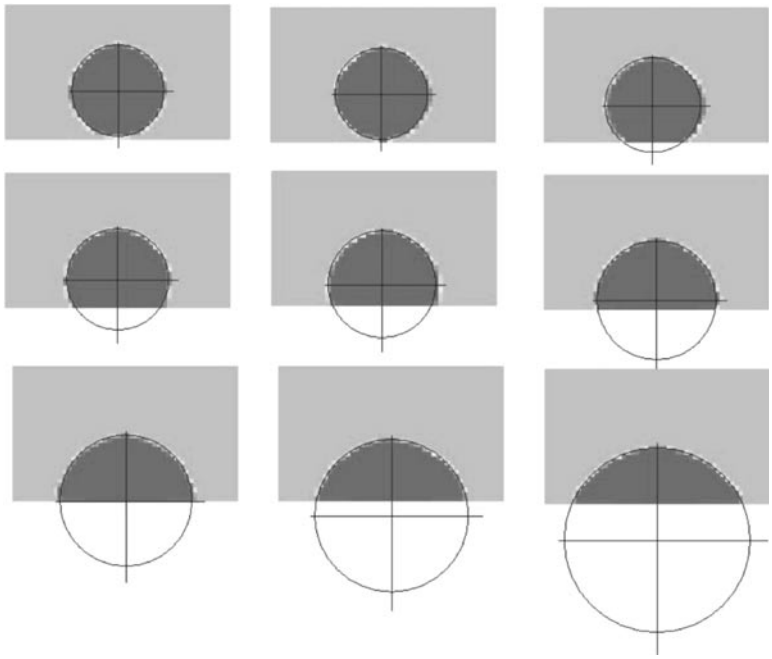

Figure 6. Results obtained for a fluid in contact with a boundary, with increasing wall wetting in 'reading order'. The collision operator in use was again $1/\tau = 1.7$ and the assumed steady state at 10^5 steps. System size was 100×80.

The results shown in figure 7 represent the flow which our model is aiming to recover. Sixty incompressible, neutrally buoyant, mutually immiscible drops of identical internal viscosity and surface tension were initialized on a lattice of size 220×50 and forced by a uniform pressure gradient. This internal geometry is broadly characteristic of the veinule

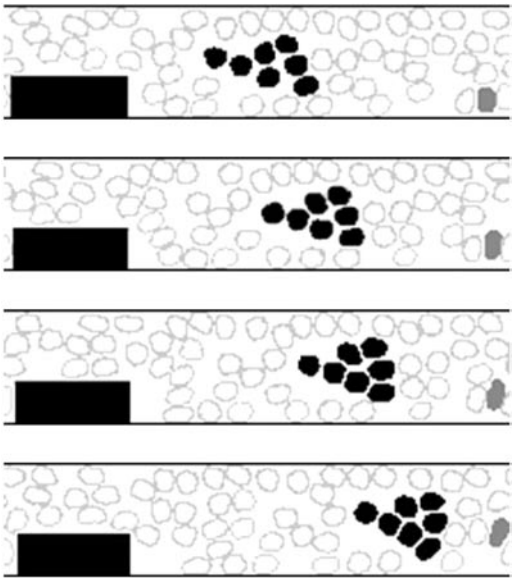

Figure 7. Incompressible, neutrally buoyant, identical, immiscible drops, initialized on a lattice, 220×50, and forced by a uniform pressure gradient (body force), in an internal geometry characteristic of the veinule microcirculation (here $Re = 20$). Periodic boundary conditions were in force left to right in this simulation. The figure shows a developing time sequence of drops, in most cases showing only the interface of each drop with the surrounding fluid; however, a cluster of drops has been completely shaded in black so as to allow the reader to track their respective positions. In addition, a trapped drop *jamming* has been highlighted.

microcirculation. Periodic boundary conditions were applied left to right. The ambient plasma fluid was set strongly to wet the boundary wall. Thus, an explicit layer of fluid was maintained between all drops and the boundary. This is a necessary precaution where no lubrication forces have been postulated, or where one wishes to avoid questions of cellular interactions at the wall. In four time frames we illustrate the jamming of one particular deforming–advecting drop (shaded grey) and the dispersion of an initially compact group (shaded black). Throughout, the role of deformation in the drops/cells is clear.

5. Conclusions

The study of some complex flows requires the explicit representation of a high density of suspended, deformable particles. The simple, tractable lattice Bhatnagar–Gross–Krook (lB) interface model advanced here is a clear improvement over preceding models, built on the basic Gunstensen algorithm [4] (figures 2 and 3). It has application to situations where it is necessary to recover only hydrodynamics of separated components. The micro-current reduction from this algorithm alone is important in opening up low Re, high Ca (*microfluidic* or surface tension dominated) flows to lB, for it is in this regime that the lB micro-current field is comparable to that of the simulated flow.

In veinule blood flow, inertial forces are more important and Ca is larger. Our application, in figure 4, demonstrates the considerable potential for modelling the advection of deformable particles. In figure 4 the drop appears to deform considerably. As an aside it follows, quite closely, a streamline of the corresponding undisturbed flow, but with considerable deformation.

That no corresponding statement seems possible when considering multiple drops, at high concentration (figure 7), is unsurprising.

With the addition of control over coalescence (evaporation) (section 3.3), our lB method also has applications to any flow containing deformable particles which can be modelled as drops, the results of figures 5 and 6, culminating in figure 7, demonstrate its ability to provide explicit information on the location of the drops and the interdependence of their motions.

Figure 7 strongly supports our controlled-coalescence lB model as the vehicle of that representation of the 'veinule' mesoscale of blood flow in which a high volume fraction of strongly interacting, advecting and deforming cells, confined by vessels of diameter comparable to the cell diameter, are modelled as non-coalescing liquid drops (section 2). The results of simulations show real potential. In figure 7 it is tempting to identify (a) 'plug flow' of drops, giving plasma-rich regions, with positive implications for the modelling of plasma skimming, (b) trapping in the primary recirculation and notably (c) the role of deformation. All these features are promising for the applications outlined in section 2. We stress that to regulate coalescence whilst controlling interfacial tension and internal drop viscosity (and hence effective particle deformability) is key in this underlying model.

The lB scheme described in this paper should be of considerable use in modelling the microcirculation. As a next step, with a simple pipe geometry, our lB model might be used quantitatively to investigate the 'phase transitions' and variations in viscosity associated with haematocrit. In this challenging application one would need, for example, explicitly to calibrate parametrization for the different fluids (to represent red, white cells, platelets, etc). However, we believe that the results presented here make the necessary investment of effort worthwhile.

References

[1] Succi S 2001 *The Lattice Boltzmann Equation for Fluid Mechanics and Beyond* (Clarendon Press) and references therein

[2] Care C M, Halliday I and Good K 2000 Lattice Boltzmann Nemato-dynamics *J. Phys. Condens. Matter* **12** 665

[3] Koponen A 1998 Simulations of fluid flow in porous media by lattice gas and lattice Boltzmann methods *PhD thesis* University of Jyvakyla, Finland

[4] Gunstensen A K, Rothman D H, Zaleski S and Zanetti G 1991 Lattice Boltzmann model of immiscible fluids *Phys. Rev.* A **43** 4320

[5] Swift M R, Osborn W R and Yeomans J M 1995 Lattice Boltzmann simulation of non-ideal fluids *Phys. Rev. Lett.* **75** 830

[6] Thompson S P, Halliday I and Care C M 1999 Mesoscopic hydrodynamics of diphasic lattice Bhatnagar–Gross–Krook fluid interfaces *Phys. Chem. Chem. Phys.* **1** 2183

[7] Shan X W and Chen H D 1994 Simulation of nonideal gases and liquid–gas phase transitions by the lattice Boltzmann equation *Phys. Rev.* E **49** 2941

[8] Benzi R, Succi S and Vergassola M 1992 The lattice-Boltzmann equation—theory and applications *Phys. Rep.* **3** 145

[9] Chen S and Doolen G D 1998 Lattice Boltzmann method for fluid flows *Ann. Rev. Fluid Mech.* **30** 329

[10] Do-Quang M, Aurell E and Vergassola M An inventory of lattice Boltzmann models of multiphase flows *Internal Report* Webpage www.psci.kth.se/Activities/Reports

[11] Damiano E R, Westheider J, Tozeren A and Ley K 1996 Variation in the velocity, deformation, and adhesion energy density of leukocytes rolling within venules *Circ. Res.* **79** 1122

[12] Quarteroni A 2001 *SIAM News* July/August **9**

[13] Caro C G, Pedeley T J, Schroter R C and Seed W A 1978 *The Mechanics of the Circulation* (Oxford: Oxford Medical Publications)

[14] Zou Q and He X Y 1997 On pressure and velocity boundary conditions for the lattice Boltzmann BGK model *Phys. Fluids* **96** 1591

[15] Zou Q, Hou S, Chen S and Doolen G D 1995 Analytical solutions of the lattice Boltzmann BGK model *J. Stat. Phys.* **81** 319

[16] Halliday I, Care C M and Thompson S P 1998 Macroscopic surface tension in a lattice Bhatnagar–Gross–Krook model of two immiscible fluids *Phys. Rev.* E **57** 514
[17] Halliday I, Hammond L A, Care C M, Good K and Stevens A 2001 Lattice Boltzmann equation hydrodynamics *Phys. Rev.* E **64** 011208
[18] Qian Y H, d'Humières D and Lallemand P 1992 Lattice BGK models for the Navier–Stokes equation *Europhys. Lett.* **17** 479
[19] Kachel V *et al* Webpage www.cyto.purdue/flowcyt/educate/ee520
[20] Dupin M M, Halliday I and Care C M (in preparation)